JOURNAL OF AIRCRAFT
Vol. 31, No. 3, May–June 1994

Inviscid Parametric Analysis of Three-Dimensional Inlet Performance

Scott D. Holland*
NASA Langley Research Center, Hampton, Virginia 23681
and
John N. Perkins†
North Carolina State University, Raleigh, North Carolina 27695

The advantages and design requirements of propulsion/airframe integration for the high Mach number flight of air-breathing vehicles have led to extensive study of the three-dimensional sidewall-compression scramjet inlet in recent years. Inlets of this genre afford a relatively simple, generic geometry while producing a highly complex, three-dimensional flowfield dominated by shock/shock and shock/boundary-layer interactions. While the importance of the viscous effects in high-speed inlet interactions is recognized, the present work addresses in a parametric fashion the inviscid effects of leading-edge sweep (between 0–70 deg) and inflow Mach number (between 2–12) on the inlet performance. Two-dimensional oblique shock theory is appropriately modified to account for the three-dimensional effects of leading-edge sweep and is applied throughout the inlet configuration to obtain inviscid shock impingement locations, mass capture, inlet compression, total pressure recovery, and kinetic energy efficiency. Comparison of these results with CFD indicates that the parametric trends are identified by this computationally quick and inexpensive method for preliminary design applications.

Nomenclature

CR = contraction ratio, W/g
Cx' = distance from throat entrance to cowl leading edge, in.
g = throat gap, in.
H = height of inlet, in.
M_N = component of inflow Mach vector normal to the shock sheet
M_1 = inflow Mach number
M_{1n} = component of inflow Mach number normal to leading edge, $M_1 \cos \Lambda$
M_{1p} = component of inflow Mach number parallel to leading edge
M_2 = resultant postshock Mach vector
M_{2n} = postshock component of Mach vector normal to leading edge in plane of wedge
M_{2p} = postshock component of Mach vector parallel to leading edge in plane of wedge
p = local static pressure, psia
p_t = local total pressure, psia
$p_{t,1}$ = inflow total pressure, psia
p_1, p_2 = static pressure upstream/downstream of shock, respectively, psia
Tx' = distance from sidewall leading edge to throat, in.
T_1, T_2 = static temperature upstream/downstream of shock, respectively, °R
W = inlet width at the sidewall leading edge, in.
x = axial distance measured from baseplate leading edge, in.
x' = axial distance measured from sidewall leading edge, in.
y = lateral distance from inlet plane of symmetry, in.
z = vertical distance from bottom surface, in.
β = angle measured in plane of wedge, deg, see Fig. 3
Γ = angle measured in plane of wedge, deg, see Fig. 3
γ = ratio of specific heats
δ = sidewall compression angle, deg
δ_{eff} = effective sidewall compression angle, measured normal to sidewall leading edge, deg
ζ = spillage angle, deg
η_{ke} = kinetic energy efficiency, $1 - \left([(p_{t1}/p_t)^{(\gamma-1)/\gamma} - 1]/\{[(\gamma - 1)/2]M_1^2\}\right)$
θ_{eff} = effective oblique shock angle, measured normal to sidewall leading edge, deg
Λ = leading edge sweep angle, deg

Introduction

INTEREST in high Mach number air-breathing propulsion (e.g., Refs. 1 and 2) has led to extensive study of scramjet engine concepts. One concept which has been under study for many years[3] employs a three-dimensional sidewall-compression scramjet inlet. Inlets of this genre were initially studied experimentally for the overall performance characteristics (at Mach numbers between 2–6) and as part of a subscale engine system.[4–7] The inlets have more recently been studied in air, helium, and tetrafluoromethane at Mach numbers between 2–22.[5,8–12] References 8 and 12 also indicate international interest in sidewall-compression inlets.

Recent work has also highlighted the use of computational fluid dynamics for inlet research. Kumar[13] has developed and evolved a three-dimensional Navier-Stokes code primarily for internal flow configurations. Favorable comparisons between experiment and computation have been presented on a generic inlet configuration at nominal Mach numbers of 4 (Ref. 14) and Mach 10 (Ref. 11). Analyses of subscale engines and combustion processes have also been performed computationally.[15–17]

Received Sept. 13, 1991; presented as Paper 92-3099 at the AIAA/SAE/ASME/ASEE 28th Joint Propulsion Conference, Nashville, TN, July 6–8, 1992; revision received May 27, 1993; accepted for publication May 27, 1993.

*Research Engineer, Experimental Hypersonics Branch, Space Systems Division, M/S 408. Member AIAA.
†Professor, Department of Mechanical and Aerospace Engineering. Associate Fellow AIAA.

Extensive study has therefore been devoted to the three-dimensional sidewall-compression scramjet inlet for a variety of test conditions. Although the swept wedge sidewalls are geometrically simple, the internal shock/shock and shock/boundary-layer interactions are inherently highly three-dimensional. A basic understanding of the configuration and global flow phenomena is a necessary foundation to the study of the complex viscous interactions presented in many of the previously mentioned studies. While the importance of the viscous effects in high-speed inlet interactions is recognized, the present work addresses in a parametric fashion the inviscid effects of leading-edge sweep (between 0–70 deg), and inflow Mach number (between 2–12) on the internal shock structure. Two-dimensional oblique shock theory is appropriately modified to account for the three-dimensional effects of leading-edge sweep and is applied throughout the inlet configuration to obtain inviscid shock impingement locations, mass capture, inlet compression, total pressure recovery, and kinetic energy efficiency. This method is demonstrated to provide a computationally inexpensive means to begin the configuration optimization process.

Configuration Description

Highly integrated propulsion systems such as those proposed for the X-30 use the vehicle forebody bow shock for external compression. The three-dimensional sidewall compression inlet (see sketch, Fig. 1) accomplishes further (internal) compression in the horizontal direction by wedge-shaped sidewalls. The leading edges of the sidewalls are swept both to reduce the aerothermal loads on the leading edges and to provide a window for spillage at the lower Mach numbers to aid in starting the inlet; the mechanism for this flow downturning (spillage) is discussed in the next section.

The sidewall compression angle δ (measured in a plane parallel to the baseplate) is commonly fixed at 6 deg as a result of a trade study,[7] a compromise between larger compression angles leading to stronger internal shocks and increased probability of boundary-layer separation and smaller compression angles leading to weaker internal shocks, but requiring the inlet to be longer to obtain the same compression, therefore imposing a size and weight penalty on the inlet. The entire compression surface is swept, culminating in a swept entrance to the throat region. The length of the swept compression surface is denoted Tx' (see Fig. 1). Since the intersection of the constant-area throat and the swept compression surface is a line swept at the leading-edge sweep angle, the length Tx' is constant regardless of the distance from the baseplate. In order to more easily compare data from various leading-edge sweep configurations, a new axial coordinate x' is introduced, where x' is the distance (measured axially) from the leading edge at any given horizontal plane. Thus, $x'/Tx' = 0.20$ represents a crossflow plane (which is also swept at the leading-edge sweep angle) located 20% of the distance between the leading edge and the throat entrance, regardless of the leading-edge sweep angle.

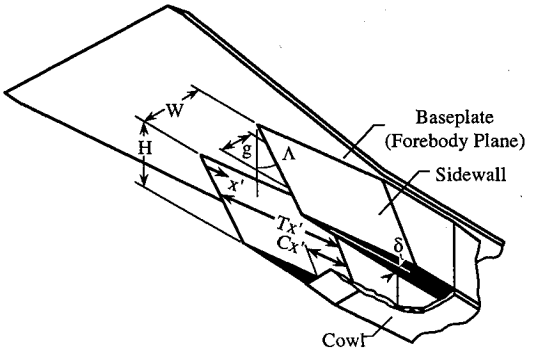

Fig. 1 Inlet model shown in flight orientation.

The contraction ratio is defined as the ratio of the entrance area to the throat area. In many studies, the height at the entrance and throat are the same so that the contraction ratio reduces to the ratio of the entrance width to the throat gap, $CR = W/g$ (see Fig. 1).

The definition of the cowl position is made simpler by the introduction of the variable Cx' (see Fig. 1), which is the distance between the cowl leading edge and the beginning of the throat region (measured in the plane of the cowl). Thus, the ratio Cx'/Tx' defines the forward extent of the cowl ahead of the throat as a percentage of the length of the compression surface. Thus, $Cx'/Tx' = 0.0$ (referred to as a 0% cowl) indicates that the cowl is at the throat, $Cx'/Tx' = 0.50$ (referred to as a 50% cowl) indicates that the cowl leading edge is located at the midpoint of the compression surface, and $Cx'/Tx' = 1.0$ (100% cowl) indicates that the cowl leading edge coincides with the sidewall leading edge.

Basic Flow Phenomena

Contraction Ratio Effects

Consider the inviscid flow past a pair of infinitely tall unswept (two-dimensional) wedges located opposite one another, i.e. an unswept inlet of infinite height. A pair of shock sheets extend from the leading edge of the wedges, cross at the centerline, and then impinge on the sidewalls. Inviscidly, the shocks cancel if they are incident at the shoulder in the throat; otherwise they continue to reflect if they strike ahead of the shoulder. Figure 2 illustrates the inviscid shock locations for the three contraction ratios considered in the present parametric study. This reflected shock pattern has been demonstrated computationally for a sidewall compression inlet of similar design in Mach 5 air (perfect gas) for a leading-edge sweep of 45 deg.[18] The inviscid shock pattern is largely dictated by δ, M_1, and CR. The sidewall compression angle and the inflow Mach number determine the inviscid shock angle through oblique shock theory. For a fixed sidewall compression angle and Mach number (and hence, fixed shock angle), the location of the shock impingement point is determined by the distance between the sidewalls, or in other words, the contraction ratio. Thus, increasing the contraction ratio (bringing the sidewalls closer together) moves the sidewall shock impingement points forward, causing the internal flow to encounter a greater number of reflected oblique shocks and increasing the compression of the inlet.

Leading-Edge Sweep Effects

The addition of leading-edge sweep to the sidewalls causes the shock sheets generated by the leading edge, the line along which the shocks intersect on the centerline, and the line along

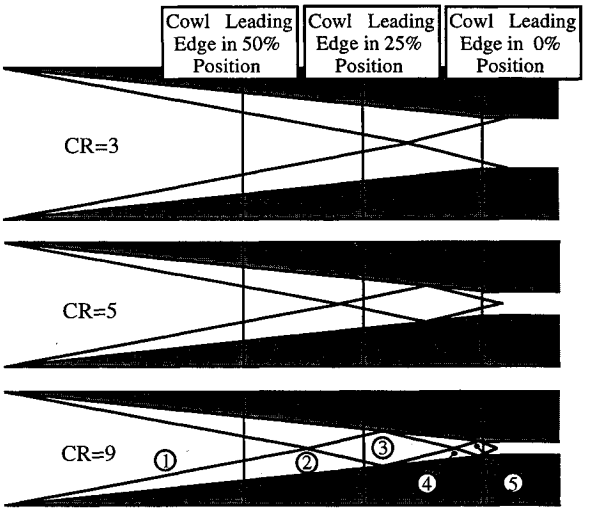

Fig. 2 Inviscid shock location predictions for $M_\infty = 10$, $\Lambda = 45$ deg, $Tx' = 9.5$ in. at contraction ratios of 3, 5, and 9.

which the shocks impinge on the sidewalls to be swept at the leading-edge sweep angle. Shock interactions of this nature occur along lines of constant leading-edge sweep angle. This trend has been demonstrated both computationally (e.g., Figs. 5 and 6 of Ref. 18 or Figs. 8.1.1b–8.1.10b of Ref. 11) and experimentally (see Figs. 7.1.1.1–20 of Ref. 11).

Sweeping the leading edges aft has an additional effect of turning the flow downward toward the cowl as the flow passes through the swept shocks. This turning is shown qualitatively by considering the inviscid flow between two infinitely long swept wedges (i.e., neglecting end effects) using oblique shock theory, modified for the inclusion of leading-edge sweep. The addition of leading-edge sweep requires that another component of the inflow Mach number (namely, the component parallel to the leading edge) be calculated through the shock. Figure 3 shows the oncoming freestream Mach vector broken into components parallel and normal to the swept wedge. Two-dimensional oblique shock theory may be applied directly to the normal component (M_{1n}) to determine its post-shock components, noting that the effective wedge angle δ_{eff}, the wedge angle measured normal to the leading edge, is given by

$$\delta_{\text{eff}} = \tan^{-1}(\tan \delta/\cos \Lambda) \tag{1}$$

and is greater than δ. The equations to find the resultant Mach vector behind the oblique shock for the two-dimensional theory may be found in several texts (e.g., Ref. 19) where three equations may be combined to give (in the notation of this study) M_{2n} in terms of M_{1n}, the ratio of specific heats, and the effective wedge and shock angles as

$$M_{2n} = \frac{\left\{ \dfrac{M_{1n}^2 \sin^2\theta_{\text{eff}} + \left[\dfrac{2}{(\gamma - 1)}\right]}{\left[\dfrac{2\gamma}{(\gamma - 1)}\right] M_{1n}^2 \sin^2\theta_{\text{eff}} - 1} \right\}^{1/2}}{\sin(\theta_{\text{eff}} - \delta_{\text{eff}})} \tag{2}$$

The parallel component M_{1p} must be treated separately. Although the component of velocity parallel to the shock remains unchanged through the shock, the Mach number associated with that velocity vector decreases due to the increase in static temperature, and therefore, the speed of sound across the shock, as

$$M_{2p} = M_{1p}(T_1/T_2)^{1/2} = M_1 \sin \Lambda (T_1/T_2)^{1/2} \tag{3}$$

With the components behind the shock known, the resultant magnitude and direction of the Mach vector can be determined. The spillage angle ζ can be determined as the difference between two angles, Γ and β, in the plane of the wedge, as shown in Fig. 3. The angle between the leading edge and the x-y plane measured in the plane of the wedge is denoted as Γ and is given by

$$\Gamma = \sin^{-1}(\sin \delta/\sin \delta_{\text{eff}}) \tag{4}$$

The angle which the resultant makes with the leading edge in the plane of the wedge β is given by

$$\beta = \tan^{-1}\left(\frac{M_{2n}}{M_{2p}}\right) = \tan^{-1}\left[\frac{M_{2n}}{(T_1/T_2)^{1/2} M_1 \sin \Lambda}\right] \tag{5}$$

The spillage angle ζ is the difference between these two angles:

$$\zeta = \Gamma - \beta = \sin^{-1}\left(\frac{\sin \delta}{\sin \delta_{\text{eff}}}\right) - \tan^{-1}\left[\frac{M_{2n}}{(T_1/T_2)^{1/2} M_1 \sin \Lambda}\right] \tag{6}$$

An alternate but equivalent definition of the spillage angle is the difference between the angle made by the resultant M_2 and its component normal to the leading-edge M_{2n} and the angle between the x-y plane and M_{2n}, both measured in the plane of the wedge (see Fig. 4). This alternate equation may be more convenient for some applications and is therefore provided for reference:

$$\zeta = \tan^{-1}(M_{2p}/M_{2n}) - \tan^{-1}(\cos \delta_{\text{eff}} \tan \Lambda) \tag{7}$$

Once the conditions behind the first shock are computed, the process is repeated for each shock upstream of the cowl leading edge. Then the total spillage and performance quantities (e.g., total pressure recovery, η_{kc}, etc.) can be computed.

Cowl Placement Effects

While spillage is important in helping the inlet start, favorable mass capture characteristics at cruise are of utmost importance for efficient operation. The flow spillage can be tempered by the position of the cowl. (The cowl leading edge is marked in Fig. 2 for each of the three cowl positions con-

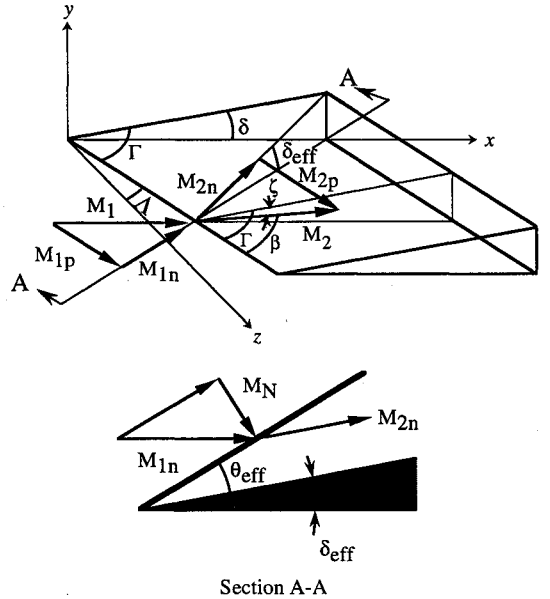

Fig. 3 Mach number components for computation of flow conditions downstream of sidewall leading-edge shock.

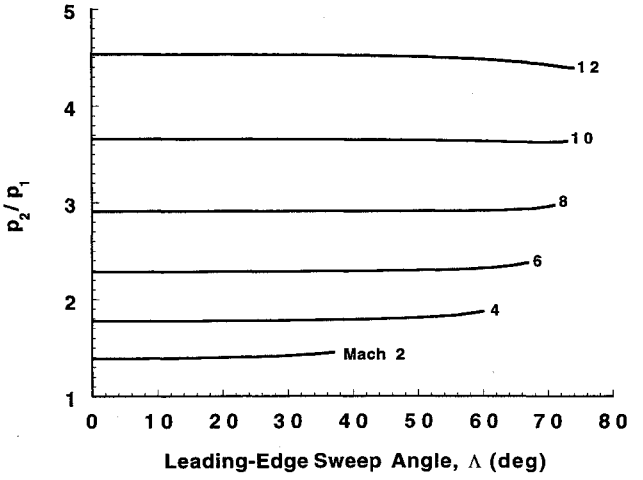

Fig. 4 Compression across leading-edge shock as a function of leading-edge sweep angle and inflow Mach number.

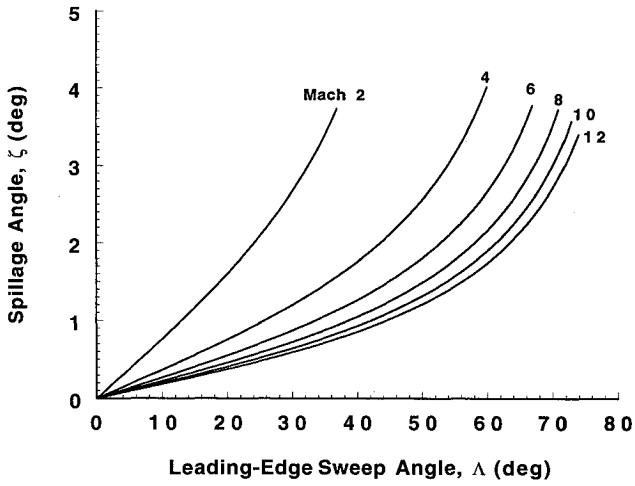

Fig. 5 Spillage angle induced by leading-edge shock as a function of leading-edge sweep angle and inflow Mach number.

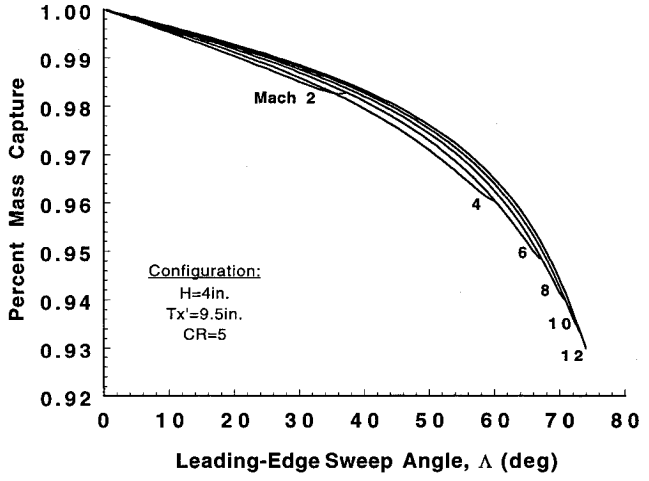

Fig. 6 Percent mass capture resulting from spillage induced by leading-edge shock as a function of leading-edge sweep angle and inflow Mach number.

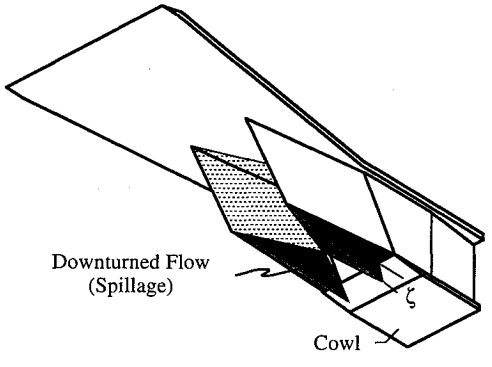

Fig. 7 Flow spillage due to swept shock sheet emanating from sidewall leading edge (spillage angle ζ is exaggerated).

sidered in the parametric study.) Compared to an aft placement, the cowl forward configuration captures more of the mass turned downward by the internal shocks. A shock develops on the cowl leading edge inside the inlet as the downturned flow impinges on the cowl and is turned back parallel to the cowl surface, further increasing the compression and decreasing the total pressure recovery of the inlet. As the cowl is placed in a progressively more forward position, it is expected that this cowl shock would influence a greater fraction of the exit plane (combustor entrance), leading to greater exit plane flow nonuniformity as well as the increased degradation of total pressure recovery.

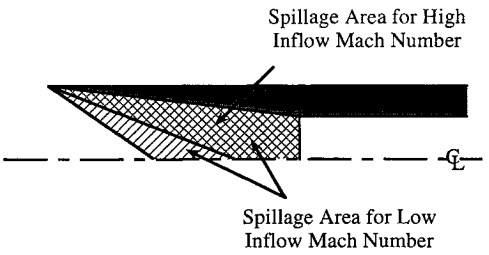

Fig. 8 Spillage area (in plane of the cowl) for low and high inflow Mach numbers.

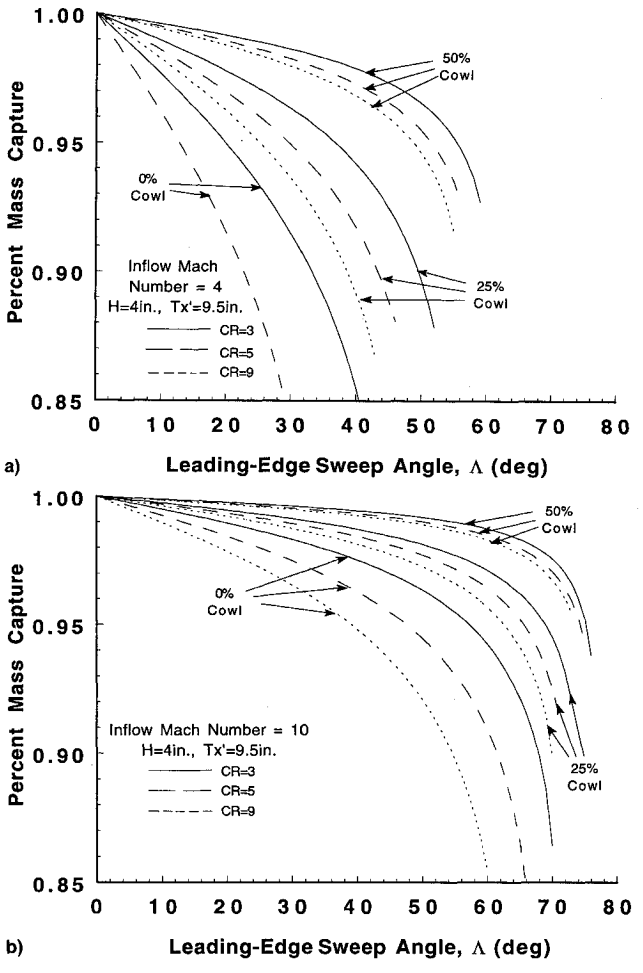

Fig. 9 Contraction ratio and cowl position effects on total mass capture: a) Mach 4 inflow, δ = 6 deg inlet and b) Mach 10 inflow, δ = 6 deg inlet.

Viscous and End Effects

While a detailed discussion of the viscous effects is beyond the scope of this article, viscous effects and end effects can play a significant (if not dominant) role in determining the internal flow structure. For instance, when the inlet height is small (compared to length), end effects can be observed to influence much of the inlet flowfield. It was noted in Ref. 20 that in the bottom 10% of the inlet, a strong downturning can be observed (particularly in the low momentum sidewall boundary layer) due to the pressure differential between the compressed postglancing shock region inside the inlet upstream of the cowl leading edge and the uncompressed flow just below the inlet. Another key feature of the internal interactions is the strong induced crossflow in the baseplate boundary layer, which has been observed to influence the flow well upstream of the glancing shocks. In some cases, the induced crossflow has led to a separation which propagates upstream of the inlet entrance (see, e.g., Ref. 11). The limitations of the present inviscid parametric analysis are ex-

Table 1 Inlet performance parameters at $M_\infty = 10$ (data taken at the cowl leading edge)

Configuration $\Lambda = 45$ deg		Percent mass capture		Throat Mach number		Total pressure recovery		Kinetic energy, efficiency, η_{ke}		p/p_1	
CR	Cowl position	Present	CFD[a]	Present	CFD	Present	CFD	Present	CFD	Present	CFD
3	50%[b]	99.3	98.0	8.8	7.8	0.89	0.67	0.998	0.994	2.0	2.9
3	0%	97.0	93.4	6.9	6.2	0.74	0.53	0.995	0.990	8.0	8.0
5	0%	95.5	91.0	5.9	5.5	0.69	0.45	0.994	0.987	19.7	17.6
9	0%	93.6	87.9	4.8	4.4	0.64	0.37	0.993	0.984	63.8	46.6

[a]Three-dimensional laminar Navier-Stokes CFD data from Ref. 11.
[b]50% Cowl data were taken in the plane located at the cowl leading edge, i.e., $x'/Tx' = 0.50$.

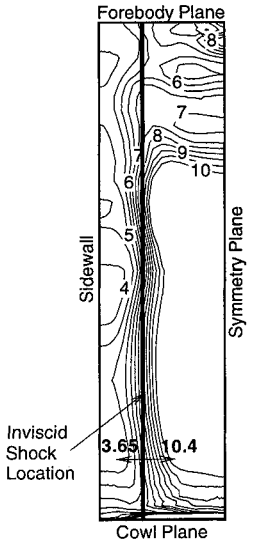

Fig. 10 Comparison of contours of inlet compression at the throat entrance from the present inviscid method with CFD from Ref. 11; inflow Mach number = 10, $\Lambda = 45$ deg, $CR = 3$, $Re = 2.15 \times 10^6$/ft, 0% cowl, $H = 4$ in., $Tx' = 9.5$ in.

plored via comparison with CFD (full three-dimensional Navier-Stokes) solutions.

Parametric Results

The effects of leading-edge sweep on the internal flow are first examined with respect to the initial shock formed on the sidewall leading edge. Then the flow conditions and shock locations are computed throughout the inlet (from the sidewall leading-edge plane to the cowl leading-edge plane) to determine the effects of leading-edge sweep on inlet performance.

With the equations thus set forth, the effects of leading-edge sweep on M_{1n}, δ_{eff}, θ_{eff}, the component of the inflow Mach number normal to the shock sheet ($M_N = M_{1n} \sin \theta_{\text{eff}}$), the leading-edge shock compression p_2/p_1, and ζ can be conveniently determined. By definition, M_{1n} decreases as the cosine of the leading-edge sweep angle. For fixed δ, the effective compression angle δ_{eff} increases with increasing Λ and is not a function of Mach number [note Eq. (1)]. The decrease in M_{1n} and the increase of the effective wedge angle δ_{eff} (and therefore θ_{eff}) with increasing Λ tend to cancel to yield a nearly constant normal Mach number, and hence inviscid shock strength. M_{1n} is observed to decrease and sin θ_{eff} to increase such that between $\Lambda = 0$ deg and $\Lambda = 60$ deg, the normal Mach number has varied by less than 0.5% at Mach 10; the compression across the leading-edge shock (p_2/p_1) is likewise invariant with leading-edge sweep angle, varying by less than 0.7% (Fig. 4). Settles and Lu[21,22] have held since the early 1980s that, based on their experimental work on the shock wave/turbulent boundary-layer interactions due to a fin, the interactions "obey a simple conical similarity rule based on inviscid shock strength irrespective of fin sweepback or angle of attack."[21] The present work demonstates that inviscidly the compensating effects of decreasing M_{1n} and increasing effective wedge angle δ_{eff} yield this invariance in shock strength with increased leading-edge sweep.

The ζ and the percent mass capture based on spillage from the first shock bay (i.e., the region labeled "2" in Fig. 2) are presented in Figs. 5 and 6, respectively. This spillage is shown three-dimensionally in Fig. 7. Since the computation of percent mass capture is configuration specific, the configuration chosen for the analysis is that of Ref. 11 (inlet height of 4 in., $Tx' = 9.5$ in.) at a contraction ratio of 5. The mass capture is observed to increase with increasing inflow Mach number for two reasons. First, the flow deflection (or spillage) angle ζ decreases with increasing Mach number, and second, since at high Mach numbers the shocks lie closer to the sidewalls, the spillage area (see Fig. 8) also decreases.

The spillage of the inlet due to all of the internal shocks upstream of the cowl leading edge has been computed, and the percent mass capture for a family of contraction ratios and cowl positions at Mach 4 and 10 is presented in Figs. 9a and 9b, respectively. It is again noted by comparing the figures that the mass capture of the entire inlet increases with increasing inflow Mach number for the previously stated reasons. The cowl position is also observed to have a strong influence on the mass capture, since a forward cowl placement prevents more of the flow turned downward by the internal glancing shocks from spilling. The contraction ratio has a less direct influence on spillage. Coupled with the inflow Mach number and the sidewall compression angle, the contraction ratio determines the number of internal reflected shocks the flow will encounter upstream of the cowl leading edge (see Fig. 2). For example, at $CR = 9$ and 25% cowl, the flow entering the inlet encounters five compressions upstream of the cowl leading edge at an inflow Mach number of 4, compared to only two compressions at an inflow Mach number of 10. Each of these compressions incrementally increases the flow deflection: ζ behind each of the five shocks for the Mach 4 inflow and $\Lambda = 45$ deg are 1.5, 2.7, 4.6, 6.4, and 9.1 deg, compared to 0.8 and 1.2 deg for the Mach 10 inflow. Thus, an increase in contraction ratio, a decrease in inflow Mach number, and an aft cowl placement are all observed to yield a decrease in the total mass capture of the inlet.

It is recognized that the viscous interactions can be significant in glancing shock/boundary-layer interactions (e.g., Refs. 11, 23–27). These interactions can impose large, localized thermal loads which affect the structural design and can also introduce significant flow nonuniformity into the combustor entrance, leading to complex fuel scheduling problems. Since the importance of these interactions limits the range of applicability of the inviscid analysis, inlet performance parameters of percent mass capture, average throat Mach number, total pressure recovery, kinetic energy efficiency, and inlet compression are compared with laminar Navier-Stokes CFD results at an inflow Mach number of 10 (Ref. 11) in Table 1. As might be expected, the magnitude of the error found in the averaged quantities grows with the number of shock interactions the flow encounters, i.e., the quantitative agreement is poorer at the higher contraction ratios. However, the parametric trends are correctly predicted. Averages of these parameters do not sufficiently reflect the complexity of the

viscous interactions nor the flow nonuniformity. Figure 10 shows contours of inlet compression (ratio of local to inflow static pressure) at the throat entrance computed for the Λ = 45 deg, CR = 3, 0% cowl configuration at $Re = 2.15 \times 10^6$/ft, and an inflow Mach number of 10 from the work of Ref. 11. Superimposed on the contour plot is the inviscid prediction based on the current method. Although the top 25% of the inlet is affected by the induced crossflow on the forebody plane (baseplate), leading to flow nonuniformity, the shock position is nominally correct (inboard 36% of the semispan). Comparison of the present results with CFD indicates that qualitatively the parametric trends and shock locations are identified by this computationally quick and inexpensive method for preliminary design applications.

Concluding Remarks

The three-dimensional sidewall compression scramjet inlet has been the subject of extensive study in recent years. The present work has provided a detailed description of a generic configuration and the inviscid internal shock structure. A summary of the inlet characteristics is as follows.

1) The present work has demonstrated that inviscidly the shock strength of a swept fin is invariant with leading-edge sweep due to the compensating effects of the decreasing normal component of the inflow Mach vector and increasing effective wedge angle (i.e., wedge angle measured normal to the sidewall leading edge). The sweep has the effect, however, of turning the flow downward, providing a window for spillage at the lower Mach numbers. This spillage is important for the inlet starting process.

2) As the inflow Mach number increases, a variable geometry characteristic is realized for a fixed geometry inlet in that the spillage window partially closes due to the internal shocks lying closer to the sidewalls. The ζ also decreased with increasing Mach number, further enhancing the capture characteristics at higher Mach numbers. Forward cowl placement can also be used to improve the mass capture by preventing some of the flow spillage.

3) Increases in contraction ratio were observed to decrease the mass capture and increase the compression by way of an increase in the number of internal shocks upstream of the cowl leading edge, each of which incrementally increased both the downward flow deflection (spillage) and local static pressure.

4) Although the quantitative agreement is poorer at the higher contraction ratios, comparison of the present inviscid results with laminar Navier-Stokes CFD results indicates that qualitative parametric trends and shock locations were identified. This work therefore provides a computationally quick and inexpensive method both for preliminary design applications and for a beginning to the optimization process for three-dimensional sidewall compression inlets over a range of hypersonic conditions.

Acknowledgments

This work was initiated while the first author was a Post-Doctoral Research Associate in the Department of Mechanical and Aerospace Engineering at North Carolina State University, supported in part by NASA Grant NCC1-153.

References

[1]Williams, R. M., "National Aero-Space Plane: Technology for America's Future," *Aerospace America*, Vol. 24, No. 11, 1986, pp. 18–22.

[2]Kandebo, S. W., "Researchers Pursue X-30 Spaceplane Technologies for 1990 Evaluation," *Aviation Week and Space Technology*, Vol. 129, No. 6, 1988, pp. 49–53.

[3]Northam, G. B., and Anderson, G. Y., "Supersonic Combustion Ramjet Research at Langley," AIAA Paper 86-1744, Jan. 1986.

[4]Trexler, C. A., "Inlet Performance of the Integrated Langley Scramjet Module (Mach 2.3 to 7.6)," AIAA Paper 75-1212, Jan. 1975.

[5]Trexler, C. A., "Tests of Two Sidewall-Compression Scramjet Inlets at Mach 18.1 to 21.6 in Helium," NASP TM 1018, May 1988.

[6]Trexler, C. A., "Inlet Starting Predictions for Sidewall-Compression Scramjet Inlets," AIAA Paper 88-3257, July 1988.

[7]Trexler, C. A., and Souders, S. W., "Design and Performance at a Local Mach Number of 6 of an Inlet for an Integrated Scramjet Concept," NASA TN D-7944, Aug. 1975.

[8]Kanda, T., Komuro, T., Masuya, G., Kudo, K., Murakami, A., Tani, K., Wakamatsu, Y., and Chinzei, N., "Mach 4 Testing of Scramjet Inlet Model," AIAA Paper 89-2680, July 1989.

[9]Holland, S. D., and Perkins, J. N., "Mach 6 Testing of Two Generic Three-Dimensional Sidewall Compression Scramjet Inlets in Tetrafluoromethane," AIAA Paper 90-0530, Jan. 1990.

[10]Holland, S. D., Hodge, J. S., and Perkins, J. N., "Wind Tunnel Blockage Study of a Generic Three-Dimensional Sidewall Compression Scramjet Inlet at Mach 10," AIAA Paper 91-0294, Jan. 1991.

[11]Holland, S. D., "A Computational and Experimental Investigation of a Three-Dimensional Hypersonic Scramjet Inlet Flow Field," Ph.D. Dissertation, North Carolina State Univ., Raleigh, NC, March 1991.

[12]Vinogradov, V., Stepanov, V., and Alexandrovich, E., "Numerical and Experimental Investigation of Airframe-Integrated Inlet for High Velocities," AIAA Paper 89-2679, July 1989.

[13]Kumar, A., "Numerical Simulation of Scramjet Inlet Flow Fields," NASA TP-2517, May 1986.

[14]Kumar, A., and Trexler, C. A., "Analysis and Performance of Scramjet Inlets Utilizing a Three-Dimensional Navier-Stokes Code. 88N14936," *Langley Symposium on Aerodynamics*, Vol. 1, pp. 187–208, NASA CP-2397, 1985.

[15]Srinivasan, S., McClinton, C. R., and Kamath, P. S., "Numerical Simulation of Flow Through the Langley Parametric Scramjet Engine," SAE Aerospace Technology Conf. and Exposition, Society of Automotive Engineers, SAE-892314, Anaheim, CA, Sept. 1989.

[16]Sekar, B., Thomas, S., and Srinivasan, S., "A Numerical Parametric Study of a Scramjet Inlet in a Mach 6 Arc Heated Test Facility," AIAA Paper 90-0531, Jan. 1990.

[17]Kumar, A., Singh, D. J., and Trexler, C. A., "Numerical Study of the Effects of Reverse Sweep on Scramjet Inlet Performance," *Journal of Propulsion and Power*, Vol. 8, No. 3, 1992, pp. 714–719; see also AIAA Paper 90-2218, July 1990.

[18]Kumar, A., "Three-Dimensional Inviscid Analysis of the Scramjet Inlet Flow Field," AIAA Paper 82-0060, Jan. 1982.

[19]Anderson, J. D., Jr., *Modern Compressible Flow*, McGraw-Hill, New York, 1982.

[20]Holland, S. D., and Perkins, J. N., "Contraction Ratio Effects in a Generic Three-Dimensional Sidewall Compression Scramjet Inlet: A Computational and Experimental Investigation," AIAA Paper 91-1708, June 1991.

[21]Settles, G. S., and Lu, F. K., "Conical Similarity of Shock/Boundary-Layer Interactions Generated by Swept and Unswept Fins," *AIAA Journal*, Vol. 23, No. 7, 1985, pp. 1021–1027.

[22]Lu, F. K., and Settles, G. S., "Conical Similarity of Shock/Boundary-Layer Interactions Generated by Swept Fins," AIAA Paper 83-1756, July 1983.

[23]Narayanswami, N., Knight, D., Bogdonoff, S. M., and Horstman, C. C., "Crossing Shock Wave-Turbulent Boundary Layer Interactions," AIAA Paper 91-0649, Jan. 1991.

[24]Batcho, P. F., Ketchum, A. C., Bogdonoff, S. M., and Fernando, E. M., "Preliminary Study of the Interactions Caused by Crossing Shock Waves and a Turbulent Boundary Layer," AIAA Paper 89-0359, Jan. 1989.

[25]Bogdonoff, S. M., and Poddar, K., "An Exploratory Study of a Three-Dimensional Shock Wave Turbulent Boundary Layer Interaction in a Corner," AIAA Paper 91-0525, Jan. 1991.

[26]Settles, G. S., and Dolling, D. S., "Swept Shock/Boundary Layer Interactions—Tutorial and Update," AIAA Paper 90-0375, Jan. 1990.

[27]Knight, D. D., Horstman, C. C., and Settles, G. S., "Three-Dimensional Shock Wave-Turbulent Boundary Layer Interactions Generated by a Sharp Fin at Mach 4," AIAA Paper 91-0648, Jan. 1991.